






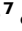

Single-cell analysis reveals a longitudinal trajectory of meningioma evolution and heterogeneity

Received: 11 September 2024

Accepted: 30 May 2025

Published online: 01 July 2025

 Check for updates

Ji Yoon Lee ^{1,2}, Eun Jung Lee^{2,3}, Bo Yeon Seo^{2,3}, Jiwon Kim ^{1,2}, Youjin Song^{1,2}, Dayoung Lee^{1,2}, Namsung Moon^{1,2}, Harim Koo ^{1,2,4}, Chul-Kee Park ⁵, Min-Sung Kim⁵, Serk In Park^{2,3,6}, Do-Hyun Nam ⁷, Doo-Sik Kong ⁷ & Jason K. Sa ^{1,2} ✉

Meningioma is the most prevalent primary brain tumor with extensive intra-tumoral heterogeneity and high recurrence rates, particularly in high-grade meningiomas. Despite advancements in understanding the molecular underpinnings of meningiomas, the longitudinal evolutionary trajectory and cellular diversity of recurrent tumors remain elusive. In this study, we perform single-nuclei sequencing of matched primary and recurrent meningiomas to explore the dynamic transcriptional heterogeneity and evolutionary trajectory of meningioma tumor cells, as well as their molecular interactions with tumor-associated immune cells that shape the complex milieu of the meningioma microenvironment. Our findings reveal that both primary and recurrent meningiomas constitute diverse cellular compositions and hierarchies, where recurrent tumor cells are characterized by enrichments of cell cycle activities and proliferative kinetics. Integrative RNA velocity and latent time uncover divergent transcriptional trajectories in recurrent tumors, demonstrating multidirectional transitions with the dominance of *COL6A3*, which confers higher risk vulnerability and treatment resistance. Tumor microenvironment analysis further reveals enrichments of *COL6A3*-mediated interactions between immunosuppressive macrophages and tumor cells in recurrent meningiomas. Collectively, these results provide profound insights into the complex evolutionary process of meningiomas and suggest potential therapeutic strategies for the treatment of recurrent tumors.

Meningioma is the most common primary central nervous system (CNS) tumor, with a prevalence of 9.51 diagnoses per 100,000 individuals¹. While the majority of meningiomas are classified as grade I benign tumors, approximately 20–30% are diagnosed as either

atypical (grade II) or anaplastic (grade III) tumors, which exhibit more aggressive and malignant phenotypes with high recurrence rates². This has led to a growing interest in investigating the unique molecular properties of meningiomas to uncover the underlying mechanisms of

¹Department of Biomedical Informatics, Korea University College of Medicine, Seoul, Republic of Korea. ²Department of Biomedical Sciences, Korea University College of Medicine, Seoul, Republic of Korea. ³Department of Biochemistry and Molecular Biology, Korea University College of Medicine, Seoul, Republic of Korea. ⁴Department of Cancer Biomedical Science, Graduate School of Cancer Science and Policy, National Cancer Center, Goyang, Republic of Korea. ⁵Department of Neurosurgery, Seoul National University College of Medicine, Seoul National University Hospital, Seoul, Republic of Korea. ⁶Department of Medicine and Center for Bone Biology, Vanderbilt University School of Medicine, Nashville, TN, USA. ⁷Department of Neurosurgery, Samsung Medical Center, Sungkyunkwan University School of Medicine, Seoul, Republic of Korea. ✉e-mail: jasonksa@korea.ac.kr

tumorigenesis and to identify potential therapeutic targets that could lead to treatment innovation.

Previous studies employing integrative genomic and transcriptomic approaches have provided profound insights into the molecular underpinnings of meningioma biology^{3–14}. These efforts have resulted in the development of a new molecular classification system that categorizes meningiomas into distinct subtypes, each characterized by unique genomic alterations. These subgroups comprise immunogenic (MG1), *NF2* wild-type (MG2), hypermetabolic (MG3), and proliferative (MG4), each defined by the activation of distinct biological pathways, such as immune response, angiogenesis, lipid metabolism, and cell cycle regulation.

In parallel, additional studies have demonstrated that meningiomas exhibit a high degree of plasticity and undergo subtype transitions between multiple cellular states^{15,16}. However, most existing analyses have predominantly focused on primary meningiomas, leaving the complex cellular hierarchy and dynamics of recurrent meningiomas relatively unexplored and therapeutically unresolved due to the limited understanding of their evolutionary trajectory. The molecular and transcriptional heterogeneity within the malignant cell populations provides meningiomas with diverse functional states that enable them to evade treatment intervention, leading to tumor recurrence and progression.

To address these unresolved aspects, we perform single-nuclei RNA sequencing (snRNA-seq) of paired primary and recurrent tumors from meningioma patients. We construct the longitudinal evolutionary trajectory of meningiomas to examine the tumor cellular states over time, identifying risk factors and potential therapeutic targets driving the malignant state of recurrent meningiomas. In addition, by analyzing the cellular composition of TME, including macrophages and lymphocytes, we provide comprehensive insights into the dynamic cellular interactions that reprogram the transcriptional states of malignant tumor cells.

Results

Longitudinal profiling of meningioma at single-cell resolution

To explore the longitudinal evolutionary trajectory of meningioma, we collected 14 matched fresh-frozen primary and recurrence samples from seven meningioma patients (Fig. 1a). Twelve matched pairs were obtained from primary and first recurrent tumors, while one pair consisted of the first and second recurrences. Three patients were diagnosed with grade I meningothelial or fibrous meningiomas, and the remaining four were diagnosed with either grade II atypical or grade III anaplastic meningiomas. All patients underwent craniotomy for tumor removal, with an average age at diagnosis of 50 years. All 14 tumor specimens were profiled using a droplet-based 10x snRNA-seq platform, resulting in a total of 100,175 cells. Of these, 74,979 cells passed the stringent quality control, with 36,601 genes detected in total (Supplementary Table S1, 2). After batch correction, cells were assigned into 11 distinct clusters, including tumor cells (37,460 cells), lymphocytes (10,779 cells), myeloid cells (24,964 cells), endothelial cells (714 cells), and additional minor populations based on high variability in gene expression profiles (Fig. 1b–d and Supplementary Table S3, 4). Tumor cells were further distinguished and verified based on copy-number variation (CNV) analysis (Fig. 1e and Supplementary Fig. S1). Tumor cells exhibited a high degree of diversity at both intra- and inter-tumoral levels, underscoring the heterogeneous nature of meningioma tumor cells^{17,18}. Non-tumor cells were predominantly intermixed across patients without notable batch effects. Tumor cells comprised the majority of the cell populations, accounting for 53.3% (19,112 out of 35,881) and 46.9% (18,348 out of 39,098) in primary and recurrent tumors, respectively (Fig. 1f). The next largest populations were macrophages (21,473 cells), followed by lymphocytes (10,479 cells). The distribution of cell types varied among patients, with dendritic cells predominantly found in primary tumors, whereas macrophages and lymphocytes were more prevalent in recurrent tumors.

Longitudinal evolutionary trajectory reveals variability in RNA velocity and increased proliferative states in recurrent meningiomas

To identify biological features constituting the unique transcriptional states of recurrent meningiomas, we performed genome-wide differential analysis between primary and recurrent tumor cells (Fig. 2a). As a result, we identified several transcriptomes actively enriched in recurrent meningiomas, including DNA repair encoding molecules (*POLQ*, *BRIPI*), cell cycle regulators (*FOXMI*) and extracellular matrix-related genes (*COL6A3*) (Fig. 2b). Pathway enrichment analysis consistently indicated that recurrent tumors were characterized by the activation of genes functionally involved in cell cycle activity, proliferation kinetics, DNA repair mechanisms, and metastasis (Fig. 2c). In contrast, primary tumors exhibited increased expression of *APOE*, *SOD3*, and *HSPA6*, which were involved in hypoxia, metabolism activity, and TNF signaling. CNV analysis highlighted consistent loss in *ARIDIA* and *NF2* genes in both primary and recurrent meningiomas, while amplification of angiogenesis-related genes such as *ROBO1* and *ROBO2* was more prevalent in recurrent tumor cells (Fig. 2d, Supplementary Fig. S2A and Supplementary Table S5). RNA velocity analysis using *velocity*¹⁹ revealed distinct gene expression dynamics between primary and recurrent meningiomas. Recurrent tumors showed significant variability in RNA velocity and latent time, characterized by multidirectional transitions and increased expression of *B2M* in the early stage, followed by a replacement with *COL6A3* in the later stage (Fig. 2e). Conversely, primary meningiomas demonstrated relatively stable velocity with a unidirectional transition from increased expression of *CCND2* to *LRP1B*.

Previous studies have defined four clinically applicable molecular classifications of meningiomas, each associated with distinct clinical outcomes and unique genomic aberrations. MG1 tumors demonstrated the most favorable prognosis with activation of immunogenic characteristics. MG2 tumors were marked by the absence of *NF2* genomic alterations, while MG3 and MG4 subtypes were defined by increased hypermetabolic and proliferative features, respectively¹⁰. We adopted these subtype transcriptional signatures to annotate all tumor cells in primary and recurrent meningiomas (Supplementary Table S6). Among the four identified molecular subtypes, MG2 tumor cells were characterized as *NF2* wild-type in both primary and recurrent tumors, as determined by inferCNV analysis (primary CNV score: 0.15, recurrent CNV score: 0.05). In contrast, the remaining subtypes collectively exhibited *NF2* loss, reinforcing that the transcriptome-based subtype classification aligns with CNV alterations (Supplementary Fig. S2B). Notably, primary tumors demonstrated a predominance of the MG1 immunogenic subtype, whereas recurrent tumors exhibited a higher proportion of MG2 (*NF2* wild-type) tumor cells (Fig. 2f). In addition, cell cycle analysis revealed a greater prevalence of proliferating cells in the S and G2M phases among recurrent tumor cells compared to primary tumors across all four subtypes (chi-square test $P < 0.001$, Fig. 2g). To investigate subtype transitions upon recurrence, we assigned the most predominant subtype within each tumor as its representative classification. Interestingly, the patient experiencing a second recurrence exhibited a pronounced shift from MG1 and MG2 to the MG3 hypermetabolism subtype, which was significantly associated with poor clinical outcomes (Supplementary Fig. S3B). Functional analysis of each molecular subtype demonstrated similarities in pathway activities between primary and recurrent tumors. MG1 subtypes showed elevated levels of various immunogenic signaling pathways, while MG2 tumors exhibited increased angiogenesis-related and hypoxia pathways (Fig. 2h). The MG3 subtype was characterized by the upregulation of metabolic pathways such as adipogenesis and fatty acid metabolism. In contrast, MG4 cells showed enrichment in cell cycle and *FOXMI*-related pathways, which have been previously recognized as major drivers in high-grade meningiomas^{20,21}. Notably, differences in pathway activities between primary and recurrent

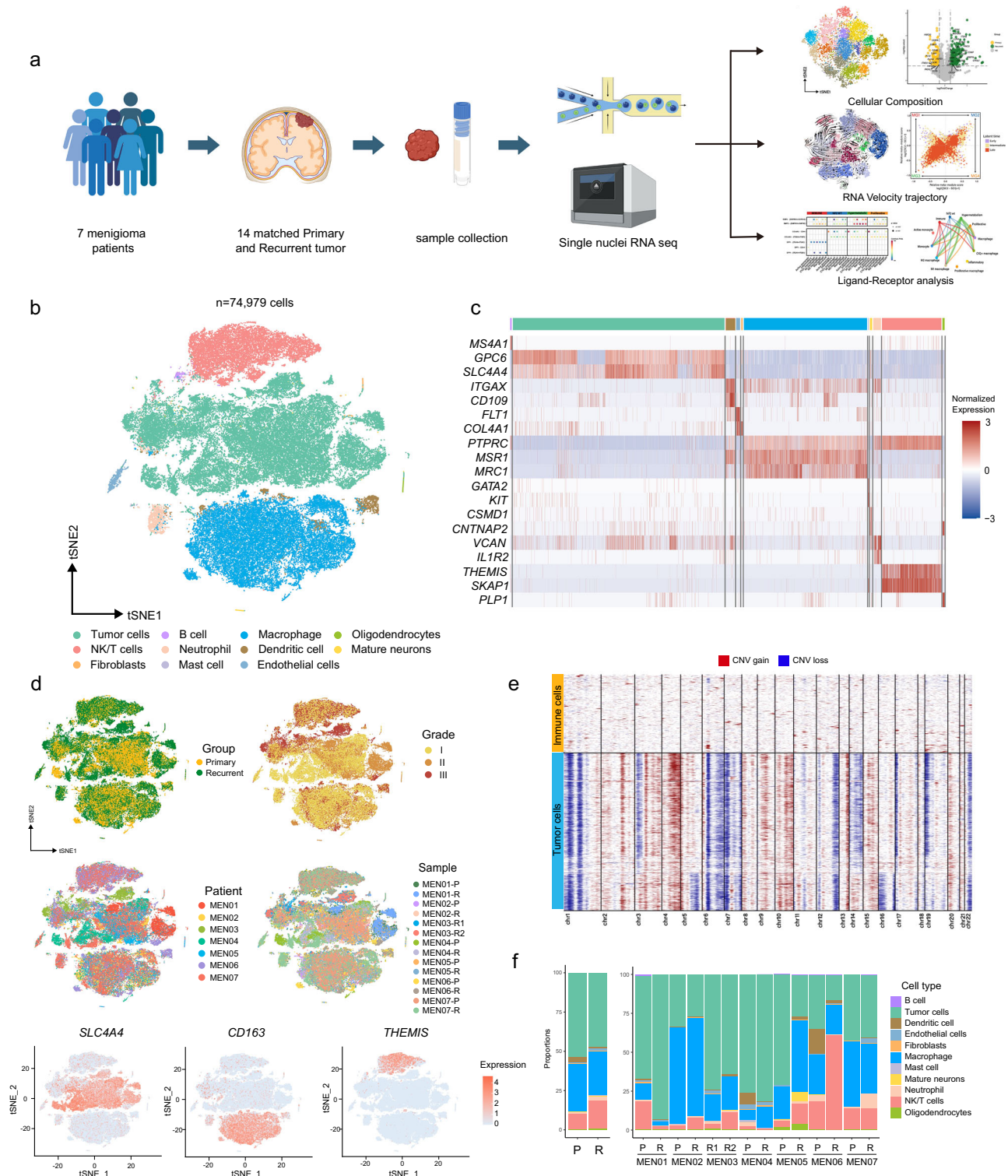
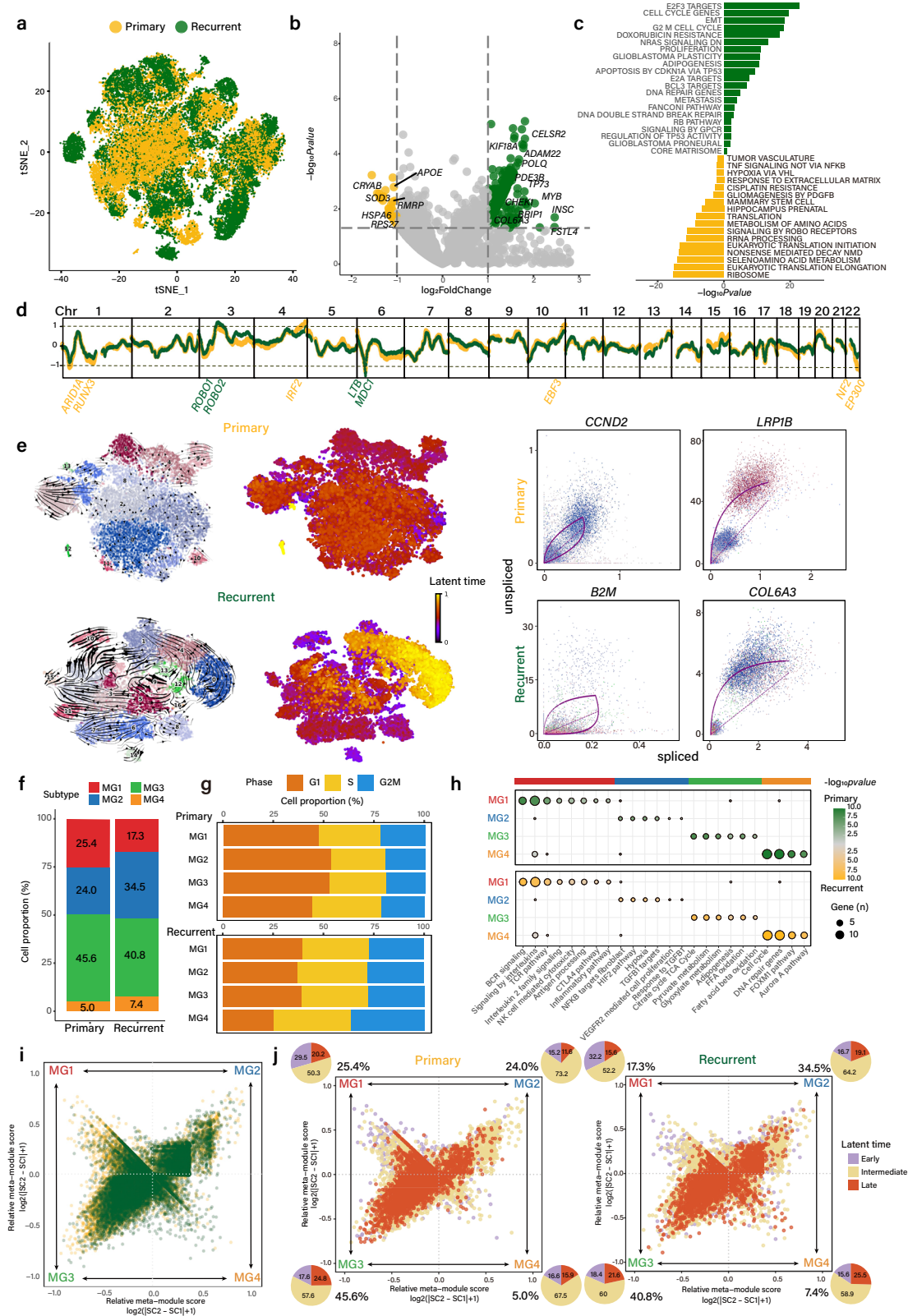


Fig. 1 | A single-cell atlas of longitudinal meningioma. a Workflow for sample collection, sequencing and analysis of 14 meningioma. Created in BioRender. Lab, S. (2025) <https://BioRender.com/pzifbd8> **b** tSNE visualization of all 74,979 cells from 14 meningioma samples with cells colored according to the corresponding cell types. **c** Heatmap for expression of marker genes in all cell types of meningioma

(left) and tSNE visualization of each marker genes (right). **d** tSNE visualization from 14 meningioma with cells colored according to the group, grade, patient, and sample. **e** CNV plot that classifies tumor cells using immune cells as a reference through inferCNV (MEN01-R sample). **f** Cell type proportion of meningioma samples on a per-sample basis. Source data are provided as a Source Data file.

meningiomas were observed for the MG3 and MG4 subtypes. MG3 recurrent tumors also showed activation of the cell cycle and mismatch repair activities, while MG4 primary tumors exhibited higher expression of the TCA cycle and adipogenesis. When we compared the subtype composition based on WHO grades in recurrent tumor cells,

we observed a higher proportion of immunogenic tumor cells in low-grade tumors, while high-grade meningiomas were marked by enrichments of hypermetabolic and proliferative tumor cells (Supplementary Fig. S4A, B). Differentially expressed gene analysis highlighted activation of *FOXMI* in high-grade meningiomas, aligning with



previous findings (Supplementary Fig. S4C). Pathway analysis consistently demonstrated enrichments of cell-cycle and EMT-related pathways in high-grade tumors. In contrast, low-grade meningiomas showed increased immune-related signals such as inflammatory response and IL6 pathways (Supplementary Fig. S4D). Cell cycle analysis further revealed a higher proportion of tumor cells in S and G2M phases in high-grade meningiomas compared to low-grade tumors

(Supplementary Fig. S3E). We also conducted a similar analysis on primary tumor cells, observing largely consistent pathway enrichment trends between primary and recurrent tumors (Supplementary Fig. S4F–H). However, we observed few key differences, particularly in pathways related to EMT and DNA repair, which were significantly enriched in the recurrent high-grade tumors but not in the primary high-grade meningiomas.

Fig. 2 | Transcriptional heterogeneity and trajectory of primary and recurrent meningioma tumor cells. **a** tSNE visualization of all 37,460 tumor cells from 14 meningioma samples colored according to the primary or recurrence status. **b** Differential gene expression analysis between primary and recurrent tumor cells (19,112 primary tumor cells and 18,348 recurrent tumor cells from 14 meningioma samples). *p*-values are from the two-sided Wald test. Source data are provided as a Source Data file. **c** Pathway enrichment analysis based on differentially expressed genes in primary and recurrent tumor cells (19,112 primary tumor cells and 18,348 recurrent tumor cells from 14 meningioma samples). *p*-values are from two-sided Fisher's exact test. **d** Copy number alteration analysis of primary and recurrent tumor cells from the inferCNV results (19,112 primary tumor cells and 18,348 recurrent tumor cells from 14 meningioma samples). **e** RNA velocity, latent time and RNA phase portraits (unspliced versus spliced) colored by cluster in primary tumor cells ($n = 19,112$) (top) and recurrent tumor cells ($n = 18,348$) (bottom). **f** Cell type proportion of tumor cells based on molecular subtypes between primary

($n = 19,112$) and recurrent ($n = 18,348$) tumor cells. Detailed cell counts are available in the Source Data file. **g** Cell type proportion of cell cycle states based on molecular subtypes between primary ($n = 19,112$) and recurrent ($n = 18,348$) tumor cells. Source data are provided as a Source Data file. **h** Pathway enrichment score across four molecular subtypes in tumor cells (19,112 primary tumor cells and 18,348 recurrent tumor cells from 14 meningioma samples). The colors represent the statistical significance (*p*-value), and the size of the node represents the number of genes in the corresponding pathways. **i, j** Two-dimensional representation of cellular subgroup of tumor cells ($n = 37,460$). Yellow dots represent primary tumor cells ($n = 19,112$), and green dots represent recurrent tumor cells ($n = 18,348$). Each quadrant corresponds to one of the molecular subtypes. The position of tumor cells (dots) reflects their relative meta-modules scores, which were derived from ssGSEA analysis of the four molecular subtypes and their colors reflect the latent time. Pie chart show proportion of latent time group (early, intermediate, and late) in each subgroup. Source data are provided as a Source Data file.

Integration of RNA velocity and latent time with subtype transcriptional signatures revealed that early-state tumor cells were predominantly observed in the immunogenic subtype (MG1) in both primary and recurrent meningiomas, while late-state cells were more prevalent in hypermetabolic (MG3) and proliferative (MG4) subtypes for primary and recurrent tumors, respectively (Fig. 2i, j and Supplementary Fig. S3A). Collectively, these findings revealed distinct cellular trajectories between primary and recurrent meningiomas and highlighted differences in molecular subtype composition that define the unique cellular profiles over the course of the disease.

Identification of *COL6A3* as a major driver of risk vulnerability and potential therapeutic target in recurrent meningioma

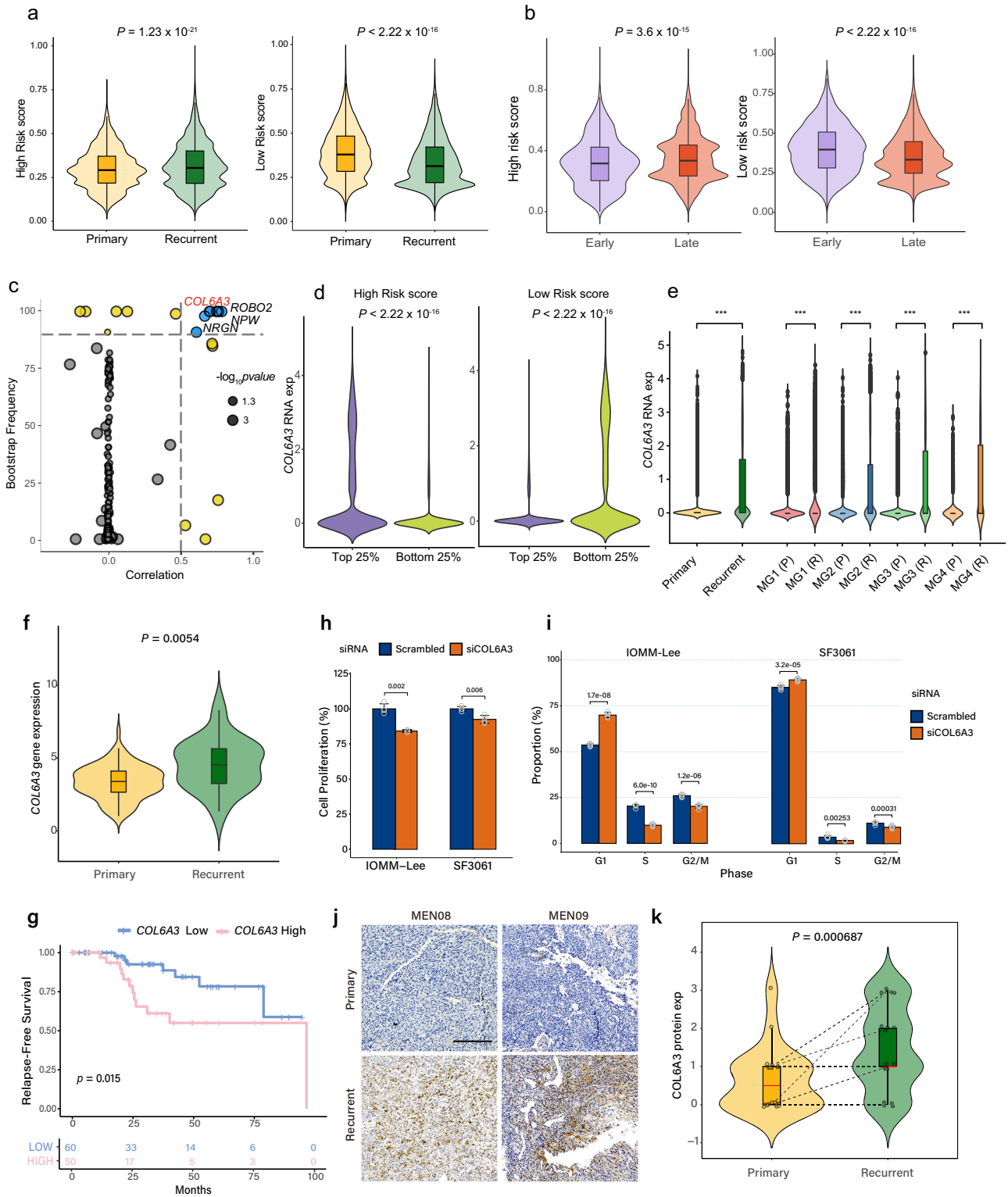
Previous studies have developed risk-associated transcriptional signatures that could aid in predicting clinical outcomes in meningioma patients using a large multi-institutional cohort²². These polygenic biomarkers successfully discriminated between patients' outcomes and demonstrated enhanced performance in predicting treatment response to radiotherapy. Leveraging both "high-risk" and "low-risk" gene signatures from prior studies, we assessed the risk states of primary and recurrent meningioma tumor cells. Notably, the "high-risk" signature was significantly upregulated in recurrent tumors, whereas the "low-risk" signature was more prevalent in primary tumors (Fig. 3a). Furthermore, the risk transcriptional signatures significantly correlated with the latent time model, where the "high-risk" score showed a strong correlation and the "low-risk" inversely correlated (Supplementary Fig. S3D). This association was particularly pronounced in primary tumor cells, where late-latent tumor cells exhibited elevated "high-risk" activity, while early-latent tumor cells were predominantly associated with "low-risk" signature (Fig. 3b). To identify molecular determinants driving increased clinical risk in recurrent meningiomas, we developed an elastic-net regression model, incorporating transcriptome data with latent time and risk signature activity. As a result, we identified a set of candidate targets, including *COL6A3*, *NPW*, and *NRGN* that were significantly associated with higher risk indications (Fig. 3c). Among these, *COL6A3* (collagen type VI alpha 3 chain), previously recognized as an essential component of extracellular matrix (ECM)^{23–26}, emerged as one of the most robust hits. Prior studies have shown that *COL6A3* promoted increased resistance to platinum-based treatments, such as cisplatin and oxaliplatin, in ovarian and breast tumors^{27–29}. Moreover, ColVI chain-encoding molecules were highly expressed in meningiomas³⁰. Comparison of *COL6A3* mRNA expression levels based on risk signature activities revealed that tumor cells with high "high-risk" scores demonstrated increased *COL6A3* expression, whereas the opposite trend was observed for "low-risk" signature scores (Fig. 3d). Furthermore, *COL6A3* exhibited a significant correlation with latent time, particularly in recurrent meningioma tumor cells (Supplementary Fig. S3E). When categorized into four distinct molecular subtypes of meningiomas (MG1, MG2,

MG3, and MG4), we discovered that tumor cells with high *COL6A3* expression levels were primarily observed in recurrent tumor cells, specifically in MG4 (proliferative) subgroup, followed by MG3 (hypermetabolism) and MG2 (*NF2* wild-type) (Fig. 3e).

Moreover, we analyzed an independent external cohort consisting of 112 meningioma RNA-seq samples from both primary and recurrent tumors¹⁴. This analysis revealed a significantly higher expression of *COL6A3* in recurrent samples compared to primary tumors (Wilcoxon test, $p = 0.0054$) (Fig. 3f). To further assess whether *COL6A3* contributes to increased recurrence vulnerability in meningiomas, we analyzed another external cohort of 110 meningioma patients with both RNA sequencing data and clinical outcomes³¹. Notably, patients with high *COL6A3* mRNA expression exhibited significantly worse relapse-free survival (RFS) probabilities (Fig. 3g). Functional validation through in vitro assays further supported these findings, as siRNA-mediated silencing of *COL6A3* significantly reduced cellular proliferation in IOMM-Lee and SF3061 meningioma cell lines (Fig. 3h). In addition, *COL6A3* knockdown led to a marked reduction in cell cycle activity, highlighting its essential role in tumor progression and proliferation (Fig. 3i). To corroborate these results, we performed immunohistochemical (IHC) staining of *COL6A3* in 18 primary and 18 recurrent samples (including 12 matched patient pairs). Consistent with our prior findings, recurrent tumors exhibited significantly higher expression levels of *COL6A3* compared to primary tumors (Fig. 3j, k). Furthermore, transcriptome analysis across three independent external cohorts (GSE183653, GSE197763, and GSE136661) confirmed that *COL6A3* expression was significantly elevated in recurrent tumors compared to primary, as well as in high-grade meningiomas (Supplementary Fig. S5A, B)^{14,32}. Collectively, these findings underscore *COL6A3*'s pivotal role in tumor progression and recurrence. Given its contribution to tumor cell proliferation and recurrence, *COL6A3* represents a promising therapeutic target for high-risk recurrent meningiomas.

TME analysis reveals cell-cell interaction between tumor cells and C1Q+ macrophages that drive *COL6A3* crosstalk in recurrent meningiomas

Next, we investigated whether cell-cell interactions between tumor cells and immune cells in the tumor microenvironment (TME) influence the cellular diversity between primary and recurrent tumors. Focusing on myeloid cells, the primary source immune cell population in the brain, we delineated the meningioma surrounding microenvironment. Myeloid cells were classified into eight distinct clusters based on unique gene expression profiles (Fig. 4a). Utilizing previously established transcriptional signatures^{10,15,33–35}, myeloid cell subpopulations were further identified as C1Q+ macrophages (*CIQA*, *CIQB*, *AIFI*), M1 macrophages (*STAT1*, *NFKB1*, *CXCL10*), M2 macrophages (*CDI163*, *MRC1*), proliferative macrophages (*BRIPI*, *MKI67*), and other defined populations. (Fig. 4b and Supplementary Table.S7). Among them, we



discovered a high prevalence of inflammatory macrophages and monocytes in primary tumors, whereas recurrent tumors exhibited higher infiltration of CIQ⁺, M1, M2, and proliferative macrophages ($P < 0.001$; Fig. 4c). Notably, the infiltration of CIQ⁺ tumor-associated macrophages (TAMs) has been associated with poor prognosis, promoting T cell exhaustion and immune tolerance induction in healthy tissues^{36–38}. Pathway analysis revealed distinct features between primary and recurrent myeloid cells, where hemostasis regulation, ECM organization, and cell cycle pathways were prominently activated in recurrent tumors (Fig. 4d). Primary tumors, on the other hand, showed

activation of pathways related to cell migration and anti-tumor responses, such as lymphocyte activation and tumor necrosis factors. To account for potential confounding sources of variation between primary and recurrent tumors, we adopted differential cell abundance analysis using *k*-nearest neighbor (KNN) based graphs. Specifically, we utilized *milor* to identify transcriptionally similar cell neighborhoods within macrophage and monocyte populations. These results further supported our findings, showing enrichments of inflammatory macrophages and monocytes in primary tumors, while CIQ⁺, M1, and M2 macrophages were identified as the primary source

Fig. 3 | Risk signature analysis of primary and recurrent tumor cells identified COL6A3 as a driver of risk vulnerability. **a** Risk score (“high-risk” and “low-risk”) comparison between primary and recurrent meningioma tumor cells ($n = 37,460$). Box plots show the median, interquartile range, and $1.5 \times$ IQR whiskers; outliers are shown as individual points. Statistical significance was assessed using the two-sided Wilcoxon rank-sum test. Source data are provided as a Source Data file. **b** Comparison of higher risk score (left) and lower risk score (right) in primary tumor cells categorized by early and late latent time groups ($n = 5,733$). Box plots show the median, interquartile range, and $1.5 \times$ IQR whiskers; outliers are shown as individual points. Statistical significance was assessed using the two-sided Wilcoxon rank-sum test. Source data are provided as a Source Data file. **c** Top genes associated with latent time identified through the elastic-net regression model. The x-axis indicates the correlation between gene expression and latent time across individual cells, and the y-axis shows the frequency of selection across 100 bootstrap iterations of the elastic-net model. p -values were calculated by Spearman correlation tests. Source data are provided as a Source Data file. **d** Expression level of *COL6A3* gene according to risk score groups. Each group of tumor cells were selected based on “high-risk” (top) or “low-risk” (bottom) signatures and termed “top 25% tumors” and “bottom 25% tumors” based on their risk signature activities. **e** Log_2 normalized gene expression level of *COL6A3* between primary and recurrent tumor cells based on molecular subtype (two-sided Wilcoxon rank-sum test). Asterisks indicate statistical significance: $p < 0.0001$ (****). **f** Violin plot showing the comparison of *COL6A3* expression levels between primary and recurrent samples in

the validation cohort ($n = 112$ samples). Box plots show the median, interquartile range, and $1.5 \times$ IQR whiskers; outliers are shown as individual points. Statistical significance was assessed using the two-sided Wilcoxon rank-sum test. **g** RFS (Relapse-Free Survival) according to *COL6A3* expression level in the validation cohort ($n = 110$). The “high” group represents patients with *COL6A3* expression that’s higher than the threshold determined by the maxstat algorithm, and the “low” group depicts patients with *COL6A3* expression lower than the threshold. Source data are provided as a Source Data file. **h** Bar plot comparing cell proliferation between siRNA-*COL6A3* and control in IOMM-Lee and SF3061 meningioma cell lines. Each bar represents the mean of $n = 4$ biological replicates, and the error bars indicate the standard deviation (SD). Source data are provided as a Source Data file. **i** Bar plot comparing the cell cycle proportion between siRNA-*COL6A3* and control in IOMM-Lee and SF3061 cell lines. Each bar represents the mean of $n = 6$ biological replicates, and the error bars indicate the standard deviation (SD). Source data are provided as a Source Data file. **j** IHC staining images of *COL6A3* in matched primary (MEN08, MEN09) and recurrent (MEN08, MEN09) meningiomas. Scale bar, 300 μm . **k** Violin plot showing the paired comparison of *COL6A3* protein expression levels between matched primary and recurrent samples through IHC staining. Box plots show the median, interquartile range, and $1.5 \times$ IQR whiskers; outliers are shown as individual points. Statistical significance was assessed using the two-sided Wilcoxon rank-sum test. A total of 18 primary and 18 recurrent samples were analyzed, including 12 matched pairs. Source data are provided as a Source Data file.

of TAM infiltration in recurrent tumors (Fig. 4e). These findings highlight that recurrent tumors are characterized by a more pronounced pro-tumorigenic potential through the infiltration of M2 and C1Q+ macrophages.

We speculated that the observed diversity in tumor cell populations between primary and recurrent tumors might result from cell-cell interactions within the TME, which could reprogram the transcriptional state of tumor cells. To explore these associations, we performed ligand-receptor analysis using *CellChat* to quantitatively assess the cellular crosstalk between tumor cells and myeloid cells. In primary tumors, the BMP5-BMPRIa signaling axis was significantly enriched between tumor cells and myeloid cells across various subtypes (Fig. 4f, g). Given its prominent role in prostate cancer, where BMPRIa promotes tumor growth while its loss impairs tumor progression, primary meningiomas are expected to exhibit similar pro-tumorigenic characteristics mediated by BMPRIa signaling. In addition, BMP signaling inhibition has been shown to disrupt M2 macrophage polarization, potentially supporting an anti-tumorigenic tumor microenvironment^{39,40}. In recurrent tumors, significant enrichment of *COL6A3*-CD44 and *COL6A3*-ITGA9/ITGB1 crosstalk between tumor cells and myeloid cells were observed. Particularly, C1Q+ macrophages were enriched in the MG2, MG3, and MG4 subtypes, corroborating our prior findings that *COL6A3* activation drives increased risk vulnerability in recurrent meningiomas. Interestingly, immunogenic recurrent meningiomas did not exhibit any significant crosstalk in the *COL6A3* signaling axis (Fig. 4f, g). To further investigate the role of *COL6A3* with C1Q+ macrophages in shaping the recurrent meningioma microenvironment, we performed IHC staining on primary and recurrent meningiomas to assess the spatial distribution of *COL6A3*, C1QA (a marker of C1Q+ macrophages), and CD163 (a marker associated with immunosuppressive macrophages) (Fig. 4h, i and Supplementary Fig. S5C, D). IHC analyses revealed significantly higher expression levels of *COL6A3* and C1QA in recurrent tumors compared to primary tumors at the protein level. This difference was particularly pronounced in matched primary-recurrent pairs, further supporting its role in tumor recurrence (Supplementary Fig. S5D).

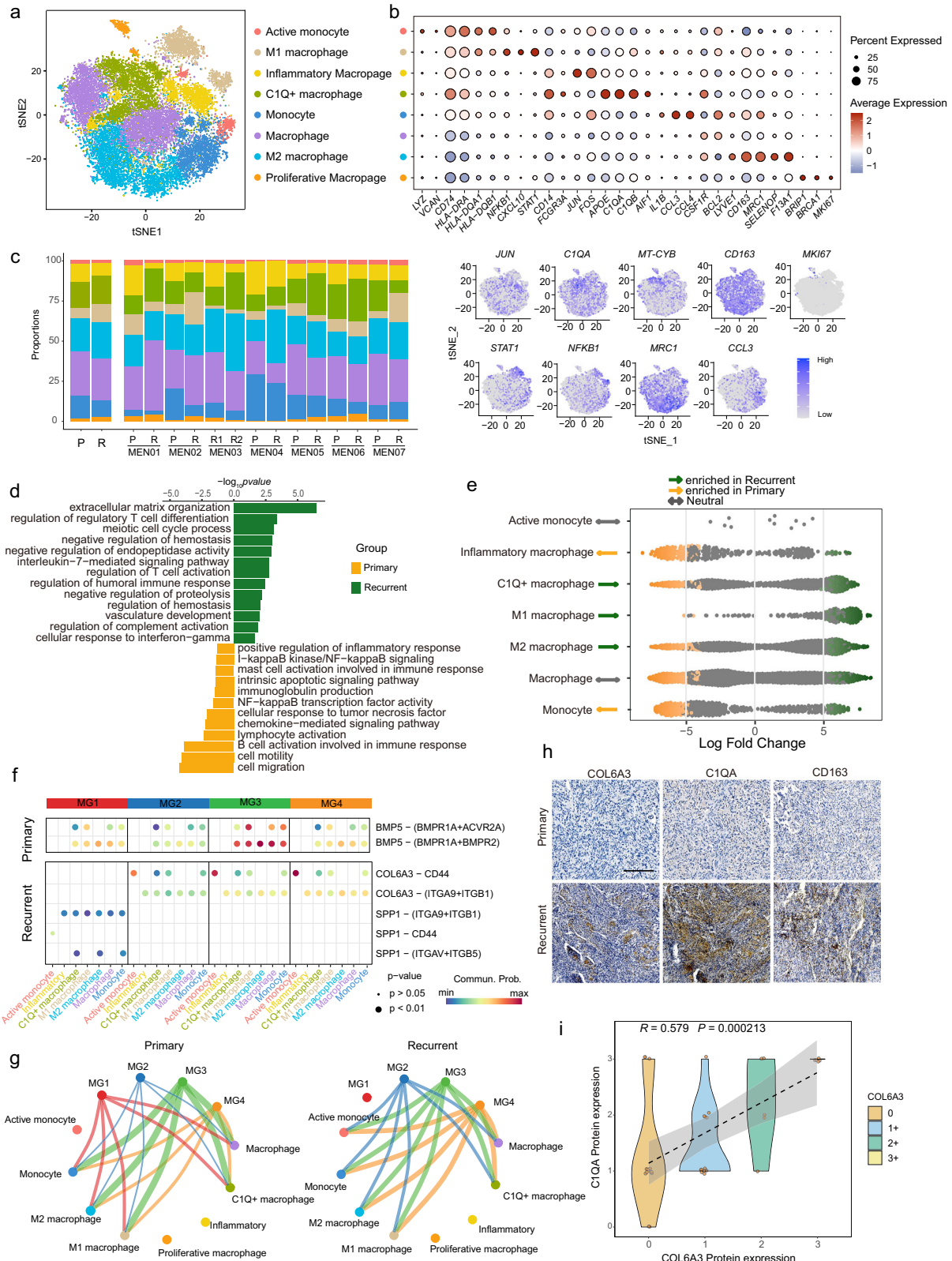
Moreover, at the individual tumor level, *COL6A3* expression was significantly correlated with C1QA, suggesting a potential interaction between *COL6A3*-expressing tumor cells and C1Q+ macrophages in the recurrent tumor microenvironment. Repolarization of M1 into M2 macrophages is mediated by multiple integrin signals, particularly integrin $\beta 7$, integrin $\alpha 9$, and integrin $\beta 1$ in a TGF β -dependent manner⁴¹. We speculate that paracrine crosstalk between tumor cells

and C1Q+ macrophages through the *COL6A3* signaling axis promotes conversion of tumor cells to a more malignant transcriptional state in recurrent meningiomas. Taken together, these findings highlight the critical role of *COL6A3*-mediated signaling in tumor progression and immune modulation, underscoring its potential as a therapeutic target for high-risk recurrent meningiomas.

Cellular architecture of lymphocytes in longitudinal meningioma

In addition to myeloid cells, we further assessed the cellular architecture of lymphocytes. We identified 14 distinct lymphocyte populations, including Natural Killer (NK) cells, CD4, and CD8 T cells, which were further subclassified based on their functional states such as CD4 regulatory T cells (*CTLA4*, *FOXP3*, *ICOS*), cytotoxic CD8 T cells (*CCL5*, *CCL4*, *GZMA*), NKG2A+ NK cells (*KLRC1*, *GZMB*, *KLRK1*)^{42–44} (Fig. 5a, b and Supplementary Table S8). Interestingly, recurrent meningiomas were characterized by increased populations of CD4 naïve and NKG2A+ CD8 T cells, while CD4 regulatory T cells and HSP+ CD4 T cells were dominant in primary tumors (Fig. 5c). Notably, infiltration of NKG2A+ NK cells was evident in high-grade recurrent meningiomas, while low-grade tumors showed increased levels of GZMK+ CD8 T cells in both primary and recurrent meningiomas. Differential gene expression analysis further revealed increased expressions of *GZMB* and *S100A8* in recurrent tumors, while heat shock protein-related genes, including *HSPA6*, *HSPA1A*, and *DUSP1*, were more abundant in primary tumors (Fig. 5d).

Gene Set Enrichment Analysis (GSEA) highlighted the activation of metabolism-related pathways, including glucose deprivation in lymphocytes from recurrent tumors, whereas primary tumors exhibited enrichments of immune memory-related pathways (Fig. 5e). In addition, lymphocytes from primary meningiomas exhibited adaptation to a hypoxic environment, while recurrent tumors showed reduced lymphocyte progenitors and diminished immune characteristics (Fig. 5f). Cell-cell interaction between tumor cells and lymphocytes demonstrated significant enrichments of crosstalk only within MG1 (immunogenic) recurrent meningiomas (Fig. 5g). Notably, immunogenic tumor cells interacted with various T cell populations through the SPP1-CD44 and SPP1-ITGA4/ITGB1 signaling axis. *SPP1* has been identified as a prognostic marker in intrahepatic cholangiocarcinoma (ICC) and is associated with poor survival⁴⁵. We speculated that recurrent tumor cells may inhibit T cell proliferation through SPP1-CD44 interactions, contributing to tumor



progression. In addition, activation of the HLA-E pathway was evident in the cell-cell interaction between tumor cells with cytotoxic CD8 T cells, NKG2A + CD8 T cells, and NKG2A + NK cells. NKG2A has been regarded as an essential immune checkpoint molecule, and prior studies have shown that tumor cells elicit CD94 and NKG2A expressions on CD8 + T cells, leading to T cell exhaustion⁴⁶. In addition, inhibition of HLA-E:CD94-NKG2A prevented pancreatic tumor

metastasis through blood circulation⁴⁷. In recurrent meningiomas, the increased presence of NKG2A + T cells suggests a unique tumor microenvironment that potentially enhances tumor malignancy and risk vulnerability through the HLA-E-NKG2A signaling axis. Collectively, these findings highlight the diverse roles of lymphocytes in shaping the unique tumor microenvironments of longitudinal meningiomas.

Fig. 4 | TME analysis reveals cell-cell interaction between tumor cells and myeloid cells in longitudinal meningioma. **a** tSNE visualization of 21,800 cells from macrophages and monocytes colored according to corresponding cell types. Detailed cell counts are available in the Source Data file. **b** Heatmap for expression of representative marker genes in myeloid cell types of meningioma ($n = 21,800$ cells)(top) and tSNE visualization of each marker genes (bottom). **c** Cell type proportion of myeloid cell ($n = 21,800$) by per-sample basis. Detailed cell counts are available in the Source Data file. **d** The pathway enrichment analysis between primary ($n = 10,776$) and recurrent ($n = 11,024$) myeloid cells. p -values are from two-sided Fisher's exact test. **e** Beeswarm plot showing the distribution of \log_2 fold change in abundance between conditions in neighborhoods from different cell type clusters ($n = 21,341$ cells). Each dot represents a neighborhood, a group of cells

clustered based on shared gene expression profiles. **f** Comparison of integral signal with input and output signals between myeloid ($n = 21,800$) and tumor cells ($n = 37,460$). Statistical significance was assessed by permutation in CellChat. **g** Circle plots showing the interactions and strengths among different cell types in primary (left) ($n = 10,776$) and recurrent ($n = 11,024$) myeloid cells (right). **h** IHC staining images of COL6A3, CIQA, and CD163 in matched primary (MEN10) and recurrent (MEN10) meningiomas. Representative images are shown; IHC performed on 36 tumor samples (18 primary meningioma and 18 recurrent meningioma samples). Scale bar, 300 μm . **i** Scatter plot showing correlation between COL6A3 and CIQA expression scores in primary ($n = 18$) and recurrent ($n = 18$) meningiomas. p -values were calculated by Spearman correlation tests. Source data are provided as a Source Data file.

Discussion

Tumor recurrence has been a long-standing challenge in the treatment of malignant brain tumors, including meningiomas^{14,48}. While the majority of meningioma diagnoses are grade I tumors, over 20% of the patients are diagnosed with high-grade meningiomas and exposed to treatment resistance and increased vulnerability to tumor relapse. Particularly, the longitudinal evolutionary trajectory of meningioma remains poorly understood, especially at single-cell resolution.

In this study, we constructed a single-cell atlas of longitudinal meningiomas to uncover the dynamic cellular composition and transcriptional heterogeneity of meningioma tumor cells and tumor-associated immune cells undergoing tumor evolution. We investigated the distinct transcriptional trajectory between primary and recurrent tumor cells, identified a driver of risk vulnerability and potential therapeutic target, and explored cell-cell interactions between tumor cells and tumor-associated immune cells within the tumor microenvironment. Our findings revealed that recurrent meningiomas exhibited activation of cell cycle and DNA repair pathways compared to matched primary tumors. Moreover, RNA velocity and latent time models indicated a predominance of hypermetabolic and proliferative tumor cells during late phases in recurrent tumors, driven by increased expression of *B2M* and *COL6A3* during early and late phases, respectively. By assessing the distinct longitudinal trajectory between primary and recurrent tumors, we developed an elastic-net regression model to identify potential therapeutic targets driving the risk vulnerability of recurrence tumors. Notably, *COL6A3* emerged as one of the most robust hits, which we further validated using external RNA-Seq cohorts of meningiomas patients and functional experiments. These findings were consistent with previous reports in colorectal cancer, pancreatic ductal adenocarcinoma, and glioblastoma, where *COL6A3* has been implicated in tumor progression, extracellular matrix remodeling, and immune evasion, further supporting its pro-tumorigenic role across multiple cancer types^{49–51}. In addition, by exploring cellular architecture in the TME, we discovered dynamic cell-cell interactions between tumor cells and immune cells, including macrophages and T cells that shape the unique tumor surroundings of primary and recurrent meningiomas. Specifically, recurrent meningiomas were characterized by infiltration of immunosuppressive macrophages, including CIQ+ and M2 macrophages. Ligand-receptor analysis revealed that COL6A3-CD44 and COL6A3-ITGA9/ITGB1 crosstalk between tumor cells and CIQ+ and M2 macrophages were highly enriched in recurrent tumors. Functional validation through immunohistochemistry (IHC) confirmed a significant upregulation of COL6A3 and CIQA in recurrent tumors, with a strong correlation between COL6A3-expressing tumor cells and CIQ+ macrophages. These findings suggest that COL6A3 interacts with CIQ+ macrophages via ITGA9 + ITGB1 integrins, shaping the distinct immune landscape of recurrent meningiomas. Integrin $\alpha 9\beta 1$ has been known to mediate interactions with ECM components and regulate immune cell adhesion, migration, and polarization⁴¹. Recent studies have indicated that COL6A3 can influence macrophage polarization toward an M2-like phenotype, promoting an immunosuppressive microenvironment⁵².

Furthermore, the C-terminal fragment of COL6A3, Endotrophin, has been implicated in modifying both tumor and immune cell behavior, potentially facilitating macrophage recruitment and functional shifts²⁶.

In addition, COL6A3-mediated signaling has been explored as a potential therapeutic target, with strategies such as blocking its interactions or modulating its expression through antisense oligonucleotide therapy currently being investigated in preclinical studies. These findings further underscore the functional role of COL6A3 in shaping a pro-tumorigenic microenvironment in recurrent tumors. In contrast, primary tumors demonstrated enrichments of inflammatory macrophages and monocytes, with the BMP5 signaling axis driving key cell-cell interactions. Focusing on lymphocytes, we observed that the SPP1-CD44 and SPP1-ITGA4/ITGB1 signaling axes were the primary interactions between immunogenic recurrent tumor cells and various lymphocytes, which we speculate to inhibit T cell proliferation. Furthermore, HLA-E crosstalk was particularly enriched between tumor cells with NKG2A+ T cells and NK cells, where NKG2A has been implicated in driving T cell exhaustion in multiple tumor types.

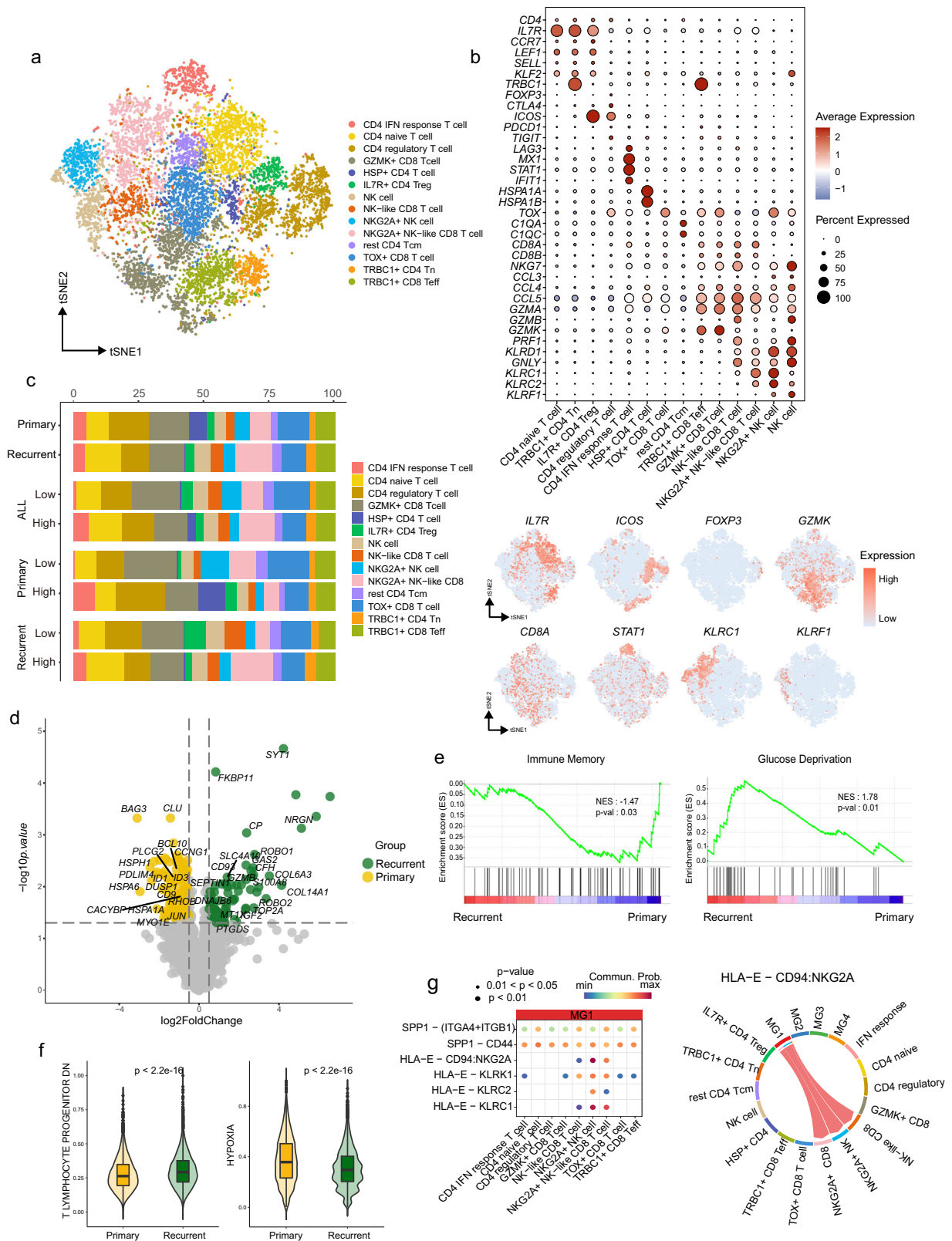
From a therapeutic perspective, targeting COL6A3 and its downstream effects offers several promising strategies. Blocking COL6A3-Integrin $\alpha 9\beta 1$ interactions could disrupt tumor-associated macrophage (TAM) recruitment and polarization, potentially reducing immunosuppressive signals within the TME. In addition, targeting COL6A3-mediated β -catenin, TGF- β /Smad signaling pathways and endotrophin inhibition also have been explored as a means to modulate fibrosis and immune suppression, positioning it as a promising target in the context of COL6A3-driven tumor progression. While direct inhibitors of COL6A3 have not yet been developed, these findings suggest that targeting COL6A3, either directly or through its interactions with integrins and macrophages, could represent a viable approach for modulating the TME and inhibiting tumor progression. Further research is warranted to explore and validate these therapeutic avenues, which could ultimately lead to the development of innovative treatments for COL6A3-driven malignancies.

In summary, our study delineates the longitudinal evolutionary trajectory of meningioma at single-cell resolution. Our results show that recurrent meningiomas are characterized by distinct transcriptional cellular states and tumor microenvironment compositions compared to primary tumors. We also observed extensive diversity in meningioma heterogeneity and evolution, with recurrent tumors evolving toward a malignant and proliferative transcriptional trajectory. Collectively, these findings advance our understanding of the mechanisms underlying longitudinal meningioma biology and high-light potential therapeutic targets for the treatment of high-risk recurrent meningioma patients.

Methods

Sample collection and processing

With appropriate approval from the institutional review board (IRB), meningioma specimens were collected from patients undergoing surgery at Samsung Medical Center. The study protocol was sanctioned by our institution's ethical committees (Samsung Medical



Center), and written informed consent was obtained from all participants.

Single-nuclei RNA-sequencing data process and analysis

To process snRNA-seq, we utilized Cell Ranger (v.5.0.0) from 10x Genomics with Count functionality for aligning reads to the prebuilt GRCh38 genome reference v.2020-A (refdata-gex-GRCh38-2020-A).

The resulting gene-by-cell unique molecular identifier (UMI) count matrix was then employed by the R package Seurat (v.4.0.5)⁵³ for subsequent analysis. Quality control measures were applied to remove barcodes falling into specific categories: those likely representing debris (expressing < 200 genes), potential doublets (expressing > 3700 genes), and cells showing signs of stress or apoptosis (with > 10% mitochondrial gene expression). Following cell

Fig. 5 | Distinctive characteristics of T cells and NK cells between primary and recurrent meningiomas. **a** tSNE visualization of 10,491 cells from T cells and NK cells colored according to corresponding cell types. Detailed cell counts are available in the Source Data file. **b** Dot plot for expression of marker genes in T cell and NK cell types of meningioma ($n = 10,491$ cells) (top) and tSNE visualization of each marker gene (bottom). **c** Cell type proportion of T cell ($n = 9395$) and NK cell ($n = 1096$) by patient and grade. Detailed cell counts are available in the Source Data file. **d** Differential gene expression comparing cells from NK/T cells between primary and recurrent meningiomas (3434 primary cells and 7057 recurrent cells). P -values are from the two-sided Wald test. Source data are provided as a Source Data file. **e** The pathway enrichment score of NK/T cells from primary ($n = 3434$) and

recurrent ($n = 7057$) tumors. p -values are from two-sided Fisher's exact test. **f** Violin plots of ssGSEA-based pathway scores across NK/T cells ($n = 10,491$). Box plots show the median, interquartile range, and $1.5 \times$ IQR whiskers; outliers are shown as individual points. Statistical significance was assessed using the two-sided Wilcoxon rank-sum test. Source data are provided as a Source Data file. **g** Comparison of Integral signal with input and output signals between NK/T cells ($n = 10,491$) and recurrent MGI tumor cells ($n = 3176$) (left) and chord diagram showing the network of HLA signaling pathways mediated only by HLA-E - CD94:NKG2A in different cell types (right). Dot color reflects communication probabilities, and dot size represents computed p -values. Statistical significance was assessed by permutation test implemented in CellChat.

filtering, raw feature counts were log-normalized, scaled, and underwent linear dimensional reduction using principal component analysis (PCA). To correct for batch effects across different samples, the Harmony (v.0.1.0) was applied to the PCA embeddings⁵⁴. Cell clusters were identified based on a K-nearest neighbor (KNN) graph model computed on Euclidean distances in PCA space, and visualization was performed using the t-distributed stochastic neighbor embedding (tSNE) algorithm. Cell type identities were assigned by performing differential gene expression analysis within each cluster and annotating based on the expression of characteristic markers.

Copy number alteration analysis

To detect large-scale chromosomal copy number variations (CNVs) using snRNA-seq data, we employed inferCNV (v.1.6.0) with default parameters recommended for 10x Genomics data⁵⁵. This analysis was conducted at the sample level using the raw counts matrix obtained after post-quality-control filtering. Prior to running inferCNV across all samples, we adjusted the bash environment with 'ulimit -s unlimited' and set specific options (expressions = 500000) within R.

Differential expression analysis

For identifying differentially expressed genes between distinct clusters, we utilized the `t.test` function in Seurat, applying multiple hypothesis correction via the Benjamini–Hochberg procedure. Genes with an adjusted p -value < 0.05 and an absolute \log_2 -fold change greater than 1 were considered differentially expressed. \log_2 -fold changes were computed based on the difference in \log_2 -transformed mean counts between groups.

RNA velocity analysis

To quantify spliced and unspliced unique molecular identifiers (UMIs) per gene per cell, we employed the Python package `velocyto`⁵⁶; followed by subsequent analyses using `scanpy` and `scvelo`¹⁹. For each cell, we computed moments (means and uncentered variances) of normalized spliced and unspliced counts using `scv.pp.moments`. RNA velocity estimation was performed with `scv.tl.velocity` using the 'dynamical' mode, and a velocity graph depicting transition probabilities was constructed using `scvelo.tl.velocity_graph`.

Molecular subtype classification

Using the molecular gene set for each subgroup from the previous study¹⁰, the ssGSEA method was applied to quantify the activity of each molecular subtype within individual tumor cells. All genes were ranked based on their expression levels, and enrichment scores for each molecular subtype were computed by calculating a running sum statistic that evaluates whether genes in each subtype gene set are enriched at the top of a ranked list compared to genes not included. This enabled quantification and comparison of the activity of the four molecular subtypes across individual tumor cells. To mitigate potential technical biases, molecular subtype scores were normalized to ensure that differences in gene set size did not skew the results.

Two-dimensional representation of meningioma subtype states
Meningioma tumor cells were first separated into Immune/NF2 WT versus Hypermetabolism/Proliferative by the sign of D , where D was calculated as:

$$D = \max(SC_{Immune}, SC_{NF2wt}) - \max(SC_{Hyper}, SC_{Pro}) \quad (1)$$

SC_x represents the single-sample gene set enrichment analysis (ssGSEA)-derived score of the corresponding molecular subtype for a given cell, measuring the enrichment level of the corresponding biological signature within that cell. The D value was used to define the y -axis of all cells.

Next, for Immune/NF2 WT cells (i.e., $D > 0$), the x -axis value was defined as:

$$\log_2(|SC_{Immune} - SC_{NF2wt}| + 1) \quad (2)$$

For Hypermetabolism/Proliferative cells (i.e., $D < 0$), the x -axis was defined as:

$$\log_2(|SC_{Hyper} - SC_{Pro}| + 1) \quad (3)$$

The resulting differences have been used to plot cells based on the corresponding quadrants representing the activity of each molecular subtype.

Feature selection using correlation with gene expression and latent time

Using `glmnet` package⁵⁷, elastic net regularization was implemented with gene expression and latent time by alpha value = 0.5 and adopted a bootstrapping strategy 100 times to obtain the top 200 genes from regression analysis. Features were selected considering their correlation values with gene expression, and latent time and the number of appearances during the bootstrapping process.

Pathway analysis

Pathway enrichment analysis was performed using the `clusterProfiler` package for functional analysis of differentially expressed genes in recurrent compared to primary meningioma. Single-sample GSEA (ssGSEA) was performed using the Easy single-cell analysis platform for enrichment (escape, version 1.9.0)⁵⁸. Enrichment scores were calculated using the `c2.all.v7.1.symbols.gmt` curated gene set.

Survival Analysis Based on COL6A3 Expression Levels

To classify high and low expression levels of COL6A3, the `maxstat` R package was applied to the bulk RNA sequencing dataset from an external cohort of 110 meningioma patients³¹. The optimal cutoff was determined using `maxstat` R package based on survival data. Survival analysis was performed to compare overall survival (OS) between patients with higher and lower COL6A3 expression using Kaplan-Meier curves and log-rank tests.

Cell culture

The human meningioma cell lines IOMM-Lee and SF3061 were kindly provided by Dr. Shin Hyuk Kang (Department of Neurosurgery, Korea University Anam Hospital), who received them from the original investigators²¹. IOMM-Lee was originally established by Dr. Wei Hua Lee⁵⁹, and SF3061 by Dr. Anitha Lal⁶⁰. Cells were regularly confirmed to be free of mycoplasma by PCR tests and authenticated for matching short tandem repeat DNA profiles of the original cell lines. The short tandem repeat profile of IOMM-Lee cell line was 100% matched with the ATCC database, whereas SF3061, which is not included in the ATCC database, was confirmed free of contamination from other cell lines. Cells were cultured in Dulbecco's Modified Eagle's Medium (DMEM; Welgene, South Korea) supplemented with 10% fetal bovine serum (FBS; Avantor, PA, USA) and 1% penicillin-streptomycin (Gibco, NY, USA). Cells were maintained at 37 °C in a humidified incubator with 5% CO₂.

Reagents and transfection

Lipofectamine™ RNAiMAX Transfection Reagent (#13778), RNase A, TRIzol® Reagent, and PowerUp SYBR™ Green Master Mix were obtained from Invitrogen (CA, USA). siRNAs used included Silencer™ Select Negative Control No.1 (#4390843) and Silencer™ Select COL6A3 siRNA (#S3318) (Invitrogen). For cell viability assays, the Premix WST-1 Cell Proliferation Assay System (TaKaRa, Japan) was used. Propidium iodide (PI; Sigma-Aldrich, MO, USA) was dissolved in PBS and used for staining. For cDNA synthesis, TOPscript™ RT DryMIX (Enzynomics, South Korea) was utilized according to the manufacturer's instructions.

siRNA Transfection

The cells were seeded (1.5×10^3 or 3×10^4 cells per well, respectively) in a 96-well or 12-well flat-bottom plate and incubated overnight. They were then transfected with siRNA using Lipofectamine RNAiMAX Transfection Reagent.

Cell proliferation assay

Seventy-two hours after transfection, 10 µL of Premix WST-1 (TaKaRa) was added to each well and the plate was incubated for 2 h. The absorbance was measured at 420 nm using a VersaMax Microplate reader (Molecular Devices)

Cell cycle assay

Twenty-four hours after transfection, the cells were cultured in serum-free medium for starvation for an additional 24 h. Subsequently, the medium was replaced with serum-containing medium for stimulation. After 6 h, the cells were harvested and fixed with ethanol at 4 °C overnight. Following fixation, the cells were washed with PBS and treated with RNase A (100 µg/mL) at 37 °C for 15 min. The cells were then stained with PI (50 µg/mL). Finally, PI-stained cells were analyzed using a BD LSRFortessa™ X-20 (BD Biosciences) and FlowJo™ software version 10.10.0.

Quantitative real-time PCR (qRT-PCR)

Forty-eight hours after transfection, the cells were harvested using TRIzol® Reagent. Total RNA was isolated following the manufacturer's user guide (Invitrogen). cDNA was synthesized using TOPscript™ RT DryMIX (enzynomics). Quantitative real-time PCR (qRT-PCR) assays were performed on a QuantStudio™ 3 system using SYBR Green master mix. The primer sequences for GAPDH were as follows: sense 5'-CATGTCGTCATGGGTGAACCA-3' and antisense 5'-AGTGATGG-CATGGACTGTGGTCAT-3'. The primer sequences for COL6A3 were as follows: sense 5'-TCTCTTAAATCAGTGCACAACG-3' and antisense 5'-AACTCTTCAACAGAGGGAAGC-3'. The results were analyzed using the 2^{-ΔΔCt} method.

Histology and immunohistochemistry

Formalin-fixed, paraffin-embedded tumor sections (4 µm) were stained with hematoxylin and eosin (H&E) and processed for immunohistochemistry (IHC). Antigen retrieval was performed using either Tris-EDTA buffer (60 °C, overnight) or 0.1% trypsin (37 °C, 30 min). Tissue sections were blocked with 3% hydrogen peroxide and 5% bovine serum albumin (BSA) in PBS. The primary antibodies used were rabbit anti-Collagen VI alpha 3 (polyclonal, MYBioSource; catalog number MBS9612481; dilution 1:100), anti-CD163 (clone EPR14643-36, Abcam; ab189915; RRID: AB_3493124; dilution 1:1000), and anti-CIQA (clone EPR14634, Abcam; ab189922; RRID: AB_2894866; dilution 1:1000). A biotinylated anti-rabbit secondary antibody (Jackson ImmunoResearch; dilution 1:1000) was applied, followed by Streptavidin-HRP (Invitrogen; dilution 1:1000) and visualization with 3,3'-diaminobenzidine (DAB; Abcam). Finally, sections were counterstained with hematoxylin. Representative images were acquired using a Zeiss AxioScan Z1 Slide Scanner, and regions of interest (ROIs) of consistent size were selected and cropped using ZEN software for downstream analysis.

Cell-cell communication analysis

To analyze cell-to-cell communication involving tumor cells and other cell types, we utilized the R package CellChat (v.1.6.1)⁶¹ with the ligand-receptor interaction database "CellChatDB.human". The default preprocessing steps were applied, and functions *computeCommunProb* and *computeCommunProbPathway* were used to infer networks for individual ligand-receptor pairs and signaling pathways.

Cell type proportion analysis using miloR

Differences in cell proportions between primary and recurrent samples were assessed using the miloR (v.1.9.1) package⁶² following a standard workflow. This involved building graphs and defining neighborhoods (similar cells identified by k-nearest neighbors (kNN)) using the *buildGraph* and *makeNhoods* functions with parameters *prop* = 0.1, *k* = 100, *d* = 30. Parameters were fine-tuned based on manual inspection of neighborhood sizes to optimize informative distributions for downstream analyses. Differential abundance within each neighborhood was evaluated using the *testNhoods* function with false discovery rate (FDR) adjustment based on neighborhood distances calculated by *calcNhhoodDistance*.

Statistics & reproducibility

Statistical analyses were conducted using R software (version 4.0.5). Differences in categorical variables (e.g., cell type proportions) were assessed using Fisher's exact test, while continuous variables were compared using Student's t-test or Wilcoxon rank-sum test, as appropriate. All hypothesis tests were two-sided, and statistical significance was set at *p* < 0.05. No statistical method was used to pre-determine sample size, and the experiments were not randomized.

Reporting summary

Further information on research design is available in the Nature Portfolio Reporting Summary linked to this article.

Data availability

The single-nucleus RNA-seq data generated in this study have been deposited in the Gene Expression Omnibus (GEO) under accession number [GSE278452](https://www.ncbi.nlm.nih.gov/geo/query/acc.cgi?acc=GSE278452). Publicly available datasets used in this study available in the GEO under accession codes [GSE183653](https://www.ncbi.nlm.nih.gov/geo/query/acc.cgi?acc=GSE183653)⁶³ [<https://www.ncbi.nlm.nih.gov/geo/query/acc.cgi?acc=GSE183653>], [GSE197763](https://www.ncbi.nlm.nih.gov/geo/query/acc.cgi?acc=GSE197763)⁶⁴ [<https://www.ncbi.nlm.nih.gov/geo/query/acc.cgi?acc=GSE197763>], [GSE136661](https://www.ncbi.nlm.nih.gov/geo/query/acc.cgi?acc=GSE136661)¹⁴ [<https://www.ncbi.nlm.nih.gov/geo/query/acc.cgi?acc=GSE136661>] and [GSE189672](https://www.ncbi.nlm.nih.gov/geo/query/acc.cgi?acc=GSE189672)³¹ [<https://www.ncbi.nlm.nih.gov/geo/query/acc.cgi?acc=GSE189672>]. Source data are provided in this paper.

Code availability

Source code can be found in the GitHub repository under: <https://github.com/jylee07/meningioma>

References

- Ostrom, Q. T. et al. CBTRUS Statistical Report: Primary brain and other central nervous system tumors diagnosed in the United States in 2013-2017. *Neuro Oncol.* **22**, iv1–iv96 (2020).
- Zhao, L. et al. An overview of management in meningiomas. *Front. Oncol.* **10**, 1523 (2020).
- Choudhury, A. et al. Hypermutated meningiomas harbor DNA methylation subgroups with distinct biological and clinical features. *Neuro Oncol.* **25**, 520–530 (2023).
- Choudhury, A. et al. Meningioma DNA methylation groups identify biological drivers and therapeutic vulnerabilities. *Nat. Genet.* **54**, 649–659 (2022).
- Olar, A. et al. Global epigenetic profiling identifies methylation subgroups associated with recurrence-free survival in meningioma. *Acta Neuropathol.* **133**, 431–444 (2017).
- Sahm, F. et al. DNA methylation-based classification and grading system for meningioma: a multicentre, retrospective analysis. *Lancet Oncol.* **18**, 682–694 (2017).
- Nassiri, F. et al. DNA methylation profiling to predict recurrence risk in meningioma: development and validation of a nomogram to optimize clinical management. *Neuro Oncol.* **21**, 901–910 (2019).
- Driver, J. et al. A molecularly integrated grade for meningioma. *Neuro Oncol.* **24**, 796–808 (2022).
- Maas, S. L. N. et al. Integrated molecular-morphologic meningioma classification: A multicenter retrospective analysis, retrospectively and prospectively validated. *J. Clin. Oncol.* **39**, 3839–3852 (2021).
- Nassiri, F. et al. A clinically applicable integrative molecular classification of meningiomas. *Nature* **597**, 119–125 (2021).
- Clark, V. E. et al. Genomic analysis of non-NF2 meningiomas reveals mutations in TRAF7, KLF4, AKT1, and SMO. *Science* **339**, 1077–1080 (2013).
- Sahm, F. et al. TERT Promoter Mutations and Risk of Recurrence in Meningioma. *J. Natl. Cancer Inst.* **108**, <https://doi.org/10.1093/jnci/djv377> (2016).
- Guyot, A. et al. Analysis of CDKN2A gene alterations in recurrent and non-recurrent meningioma. *J. Neurooncol.* **145**, 449–459 (2019).
- Patel, A. J. et al. Molecular profiling predicts meningioma recurrence and reveals loss of DREAM complex repression in aggressive tumors. *Proc. Natl. Acad. Sci. USA* **116**, 21715–21726 (2019).
- Wang, A. Z. et al. Single-cell profiling of human dura and meningioma reveals cellular meningeal landscape and insights into meningioma immune response. *Genome Med.* **14**, <https://doi.org/10.1186/s13073-022-01051-9> (2022).
- Fan, H. L. et al. Decoding meningioma heterogeneity and neoplastic cell-macrophage interaction through single-cell transcriptome profiling across pathological grades. *J. Transl. Med.* **21**, <https://doi.org/10.1186/s12967-023-04445-4> (2023).
- Vasudevan, H. N. et al. Intratumor and informative heterogeneity influence meningioma molecular classification. *Acta Neuropathol.* **144**, 579–583 (2022).
- Magill, S. T. et al. Multiplatform genomic profiling and magnetic resonance imaging identify mechanisms underlying intratumor heterogeneity in meningioma. *Nat. Commun.* **11**, 4803 (2020).
- Bergen, V., Lange, M., Peidli, S., Wolf, F. A. & Theis, F. J. Generalizing RNA velocity to transient cell states through dynamical modeling. *Nat. Biotechnol.* **38**, 1408–1414 (2020).
- Vasudevan, H. N. et al. Comprehensive molecular profiling identifies FOXM1 as a key transcription factor for meningioma proliferation. *Cell Rep.* **22**, 3672–3683 (2018).
- Kim, H. et al. Forkhead box M1 (FOXM1) transcription factor is a key oncogenic driver of aggressive human meningioma progression. *Neuropathol. Appl. Neurobiol.* **46**, 125–141 (2020).
- Chen, W. C. et al. Targeted gene expression profiling predicts meningioma outcomes and radiotherapy responses. *Nat. Med.* **29**, 3067–3076 (2023).
- Lu, P., Weaver, V. M. & Werb, Z. The extracellular matrix: a dynamic niche in cancer progression. *J. Cell Biol.* **196**, 395–406 (2012).
- Fitzgerald, J. et al. The N-terminal N5 subdomain of the alpha 3(VI) chain is important for collagen VI microfibril formation. *J. Biol. Chem.* **276**, 187–193 (2001).
- Lamande, S. R., Morgelin, M., Adams, N. E., Selan, C. & Allen, J. M. The C5 domain of the collagen VI alpha3(VI) chain is critical for extracellular microfibril formation and is present in the extracellular matrix of cultured cells. *J. Biol. Chem.* **281**, 16607–16614 (2006).
- Wang, J. & Pan, W. The biological role of the collagen alpha-3 (VI) chain and its cleaved C5 domain fragment endotrophin in cancer. *Onco Targets Ther.* **13**, 5779–5793 (2020).
- Sherman-Baust, C. A. et al. Remodeling of the extracellular matrix through overexpression of collagen VI contributes to cisplatin resistance in ovarian cancer cells. *Cancer Cell* **3**, 377–386 (2003).
- Park, J., Morley, T. S. & Scherer, P. E. Inhibition of endotrophin, a cleavage product of collagen VI, confers cisplatin sensitivity to tumours. *Embo Mol. Med.* **5**, 935–948 (2013).
- Varma, R. R. et al. Gene expression profiling of a clonal isolate of oxaliplatin resistant ovarian carcinoma cell line A2780/C10. *Oncol. Rep.* **14**, 925–932 (2005).
- Sharma, S. et al. Multipronged quantitative proteomic analyses indicate modulation of various signal transduction pathways in human meningiomas. *Proteomics* **15**, 394–407 (2015).
- JCT, B. ayley et al. Multiple approaches converge on three biological subtypes of meningioma and extract new insights from published studies. *Sci. Adv.* **8**, eabm6247 (2022).
- Choudhury A, et al. Perivascular NOTCH3+ Stem Cells Drive Meningioma Tumorigenesis and Resistance to Radiotherapy. *Cancer Discov* **14**, 1823–1837 (2024).
- Pombo Antunes, A. R. et al. Single-cell profiling of myeloid cells in glioblastoma across species and disease stage reveals macrophage competition and specialization. *Nat. Neurosci.* **24**, 595–610 (2021).
- Chen, Y. P. et al. Single-cell transcriptomics reveals regulators underlying immune cell diversity and immune subtypes associated with prognosis in nasopharyngeal carcinoma. *Cell Res.* **30**, 1024–1042 (2020).
- Villani, A. C. et al. Single-cell RNA-seq reveals new types of human blood dendritic cells, monocytes, and progenitors. *Science* **356**, <https://doi.org/10.1126/science.aah4573> (2017).
- Zhang, Q. et al. Landscape and dynamics of single immune cells in hepatocellular carcinoma. *Cell* **179**, 829–845 (2019).
- Huang, H. et al. Prognostic implications of the complement protein C1q and its correlation with immune infiltrates in Osteosarcoma. *Onco Targets Ther.* **14**, 1737–1751 (2021).
- Yang, J. et al. Integrated genomic and transcriptomic analysis reveals unique characteristics of hepatic metastases and prometastatic role of complement C1q in pancreatic ductal adenocarcinoma. *Genome Biol.* **22**, 4 (2021).
- Owens, P. et al. Inhibition of BMP signaling suppresses metastasis in mammary cancer. *Oncogene* **34**, 2437–2449 (2015).
- Valencia, J. et al. Acute Lymphoblastic Leukaemia cells impair dendritic cell and macrophage differentiation: Role of BMP4. *Cells* **8**, <https://doi.org/10.3390/cells8070722> (2019).
- Deng, M. et al. Modification of PLGA Scaffold by MSC-derived extracellular matrix combats macrophage inflammation to initiate bone regeneration via TGF-beta-induced protein. *Adv. Health. Mater.* **10**, e2100872 (2021).

42. Anandasabapathy, N. et al. Flt3L controls the development of radiosensitive dendritic cells in the meninges and choroid plexus of the steady-state mouse brain. *J. Exp. Med.* **208**, 1695–1705 (2011).
43. Mrdjen, D. et al. High-dimensional single-cell mapping of central nervous system immune cells reveals distinct myeloid subsets in health, aging, and disease. *Immunity* **48**, 599 (2018).
44. Van Hove, H. et al. A single-cell atlas of mouse brain macrophages reveals unique transcriptional identities shaped by ontogeny and tissue environment. *Nat. Neurosci.* **22**, 1021–1035 (2019).
45. Cheng, M. et al. Immunosuppressive role of SPP1-CD44 in the tumor microenvironment of intrahepatic cholangiocarcinoma assessed by single-cell RNA sequencing. *J. Cancer Res. Clin. Oncol.* **149**, 5497–5512 (2023).
46. Sheu, B. C. et al. Up-regulation of inhibitory natural killer receptors CD94/NKG2A with suppressed intracellular perforin expression of tumor-infiltrating CD8+ T lymphocytes in human cervical carcinoma. *Cancer Res.* **65**, 2921–2929 (2005).
47. Liu, X. et al. Immune checkpoint HLA-E:CD94-NKG2A mediates evasion of circulating tumor cells from NK cell surveillance. *Cancer Cell* **41**, 272–287 (2023).
48. Kim, K. H. et al. Integrated proteogenomic characterization of glioblastoma evolution. *Cancer Cell* **42**, 358–377 (2024).
49. Liu, W., Li, L., Ye, H., Tao, H. & He, H. Role of COL6A3 in colorectal cancer. *Oncol. Rep.* **39**, 2527–2536 (2018).
50. Arafat, H. et al. Tumor-specific expression and alternative splicing of the COL6A3 gene in pancreatic cancer. *Surgery* **150**, 306–315 (2011).
51. Cha, J. et al. Collagen VI deposition primes the glioblastoma microenvironment for invasion through mechanostimulation of beta-catenin signaling. *PNAS Nexus* **3**, pga355 (2024).
52. Meng, Z. et al. Exploring the immune infiltration landscape and M2 macrophage-related biomarkers of proliferative diabetic retinopathy. *Front. Endocrinol.* **13**, 841813 (2022).
53. Butler, A., Hoffman, P., Smibert, P., Papalexi, E. & Satija, R. Integrating single-cell transcriptomic data across different conditions, technologies, and species. *Nat. Biotechnol.* **36**, 411–420 (2018).
54. Korsunsky, I. et al. Fast, sensitive and accurate integration of single-cell data with Harmony. *Nat. Methods* **16**, 1289–1296 (2019).
55. Patel AP, et al. Single-cell RNA-seq highlights intratumoral heterogeneity in primary glioblastoma. *Science* **344**, 1396–1401 (2014).
56. La Manno, G. et al. RNA velocity of single cells. *Nature* **560**, 494–498 (2018).
57. Friedman, J., Hastie, T. & Tibshirani, R. Regularization paths for generalized linear models via coordinate descent. *J. Stat. Softw.* **33**, 1–22 (2010).
58. Borcherding, N. et al. Mapping the immune environment in clear cell renal carcinoma by single-cell genomics. *Commun. Biol.* **4**, 122 (2021).
59. Lee, W. H. Characterization of a newly established malignant meningioma cell line of the human brain: IOMM-Lee. *Neurosurgery* **27**, 389–395 (1990).
60. Baia, G. S. et al. A genetic strategy to overcome the senescence of primary meningioma cell cultures. *J. Neurooncol.* **78**, 113–121 (2006).
61. Jin, S. et al. Inference and analysis of cell-cell communication using CellChat. *Nat. Commun.* **12**, 1088 (2021).
62. Dann, E., Henderson, N. C., Teichmann, S. A., Morgan, M. D. & Marioni, J. C. Differential abundance testing on single-cell data using k-nearest neighbor graphs. *Nat. Biotechnol.* **40**, 245–253 (2022).
63. Choudhury, A. et al. Perivascular NOTCH3+ stem cells drive meningioma tumorigenesis and resistance to radiotherapy. *Cancer Discov.* **14**, 1823–1837 (2024).
64. Pre-clinical validation of an RNA-based precision oncology platform for patient-therapy alignment in a diverse set of human malignancies resistant to standard treatments. (2022).

Acknowledgements

This research was supported by a grant from the Korea Health Technology R&D Project through the Korea Health Industry Development Institute, funded by the National Research Foundation of Korea (NRF) grant funded by the Korean government (MSIT) (RS-2023-00209742). This research was also supported by the MSIT (Ministry of Science and ICT), Korea, under the ICAN (ICT Challenge and Advanced Network of HRD) program (IITP-2024-RS-2022-00156439) supervised by the IITP (Institute of Information & Communications Technology Planning & Evaluation). We thank Professor Shin Hyuk Kang for generously providing the cell line used in this study. The workflow for sample collection, sequencing, and analysis in Fig.1a was created with BioRender.com.

Author contributions

J.K.S. conceived, designed, and supervised the study. J.Y.L. performed the majority of the bioinformatics analysis with help from J.K., Y.S., D.L., N.M., and H.K. C.K.P., M.S.K., D.H.N., and D.S.K. provided surgical specimens and interpreted clinical data. E.J.L., B.Y.S., and S.I.P. performed in vitro assays. J.Y.L. wrote the original manuscript. J.K.S. reviewed and edited the manuscript. All authors read and approved the final manuscript.

Competing interests

The authors declare no competing interests.

Ethics approval and consent to participate

The research conformed to the principles of the Declaration of Helsinki.

Additional information

Supplementary information The online version contains supplementary material available at <https://doi.org/10.1038/s41467-025-60653-0>.

Correspondence and requests for materials should be addressed to Jason K. Sa.

Peer review information *Nature Communications* thanks Stephen Magill, and the other anonymous reviewer(s) for their contribution to the peer review of this work. A peer review file is available.

Reprints and permissions information is available at <http://www.nature.com/reprints>

Publisher's note Springer Nature remains neutral with regard to jurisdictional claims in published maps and institutional affiliations.

Open Access This article is licensed under a Creative Commons Attribution-NonCommercial-NoDerivatives 4.0 International License, which permits any non-commercial use, sharing, distribution and reproduction in any medium or format, as long as you give appropriate credit to the original author(s) and the source, provide a link to the Creative Commons licence, and indicate if you modified the licensed material. You do not have permission under this licence to share adapted material derived from this article or parts of it. The images or other third party material in this article are included in the article's Creative Commons licence, unless indicated otherwise in a credit line to the material. If material is not included in the article's Creative Commons licence and your intended use is not permitted by statutory regulation or exceeds the permitted use, you will need to obtain permission directly from the copyright holder. To view a copy of this licence, visit <http://creativecommons.org/licenses/by-nc-nd/4.0/>.

© The Author(s) 2025